Engendering Unprecedented Activation of Oxygen Evolution via Rational Pinning of Ni Oxidation State in Prototypical Perovskite: Close Juxtaposition of Synthetic Approach and Theoretical Conception

Rebecca Pittkowski, Spyridon Divanis, Mariana Klementová, Roman Nebel, Shahin Nikman, Harry Hoster, Sanjeev Mukerjee, Jan Rossmeisl, and Petr Krtil*

ACCESS | Metrics & More | Article Recommendations | SI Supporting Information

ABSTRACT: Rational optimization of the OER activity of catalysts based on $LaNiO_3$ oxide is achieved by maximizing the presence of trivalent Ni in the surface structure. DFT investigations of the $LaNiO_3$ catalyst and surface structures related to it predict an improvement in the OER activity for these materials to levels comparable with the top of the OER volcano if the La content is minimized while the oxidation state of Ni is maintained. These theoretically predicted structures of high intrinsic OER activity can be prepared by a templated spray-freeze freeze-drying synthesis followed by a simple postsynthesis exfoliation-like treatment in acidic media. These nanocrystalline $LaNiO_3$-related materials confirm the theoretical predictions, showing a dramatic improvement in OER activity. The exfoliated surfaces remain stable in OER catalysis, as shown by an in-*operando* ICP-OES study. The unprecedented OER activation of the synthesized $LaNiO_3$-based materials is related to a close juxtaposition of the theoretical conception of ideal structural motifs and the ability to engender such motifs using a unique synthetic procedure, both principally related to stabilization and pinning of the Ni oxidation state within the local coordination environment of the perovskite structure.

KEYWORDS: electrocatalysis, oxygen evolution, rational catalyst design, DFT
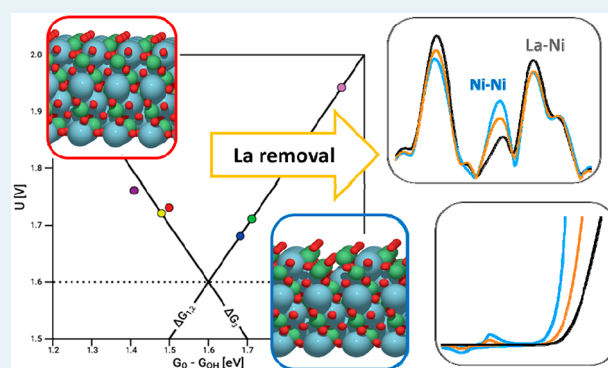
INTRODUCTION

Replacing fossil fuels as the main energy carrier by renewable electricity sources is one of the most urgent challenges for science and technology.[1] While the technologies for renewable electricity generation are relatively advanced, their intermittent nature brings up the question of the reversible storage of renewable electricity in chemical bonds.[2] "Green" hydrogen produced from water electrolysis is expected to play a major role as such an energy storage option.[3,4] It is generally known that the efficiency of the water electrolysis is in fact controlled by a sluggish oxygen evolution (OER) while the hydrogen evolution reaction (HER) taking place at the cathode can be optimized and scaled up with less difficulty.[5] Hence, the design of oxygen-evolving catalysts has turned into one of the major topics in electrocatalysis. Although the most efficient water electrolyzers are based on polymer electrolyte membrane (PEM) cells operating in highly acidic media,[4,6] their applicability is restricted by the lack of stable and feasible catalyst materials.[7,8] This stresses the potential of the alkaline electrolyzers, which despite lower efficiency can rely on

catalysts based on more abundant transition-metal oxides: e.g. Mn, Ni, Fe, and Co.[9−11]

Namely, the Ni-based catalysts have become highly popular, thanks to the abundance of nickel. The oxygen evolution on Ni-based compounds is inherently connected with the formation of trivalent nickel under *operando* conditions.[12−15] Ni-based perovskite oxides with the stoichiometry ABO_3, where the A-sites are occupied by alkaline-earth or rare-earth cations and the B-sites are occupied with Ni, represent in this context attractive candidates for the oxygen evolution catalysis in alkaline electrolytes.[16−19] It ought to be stressed that the variability of the perovskite structure (i.e., the possibility to combine different A-site and B-site cations) facilitates control
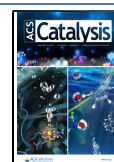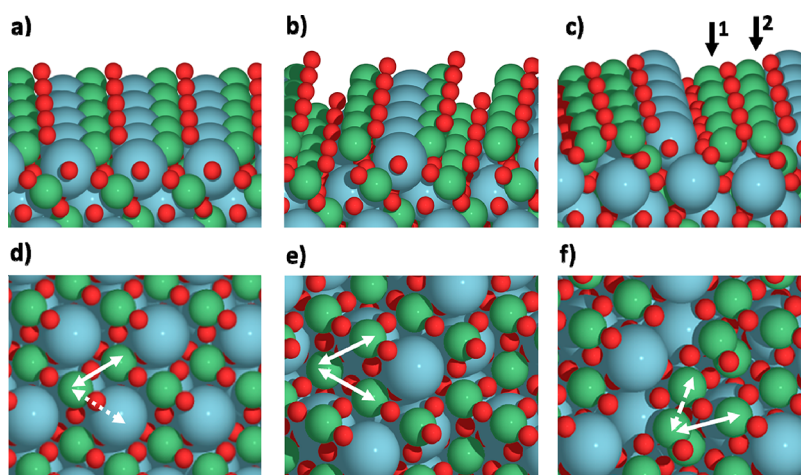
Figure 1. Geometry optimized structures of (a) stoichiometric LaNiO$_3$ perovskite, (b) La-depleted LaNiO$_3$ structure before recombination, and (c) La-depleted LaNiO$_3$ structure after recombination, with Ni in two different arrangements (marked with arrows, 1 and 2) being tested as the active site for OER in this example. Surface structures of (d) the stoichiometric LaNiO$_3$ perovskite, Ni–Ni (3.7 Å, solid arrow), La–Ni (3.3 Å, dotted arrow), (e) the La-depleted surface before recombination, Ni–Ni (3.5 Å, solid arrows), and (f) the exposed nickel surface after recombination, showing two different Ni–Ni distances: 2.8 Å (dashed arrow) and 3.5 Å (solid arrow).
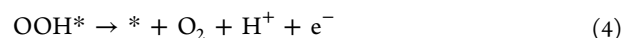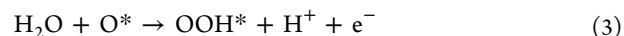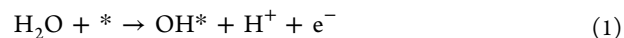
of the oxidation state of the B-site cation. Combining theory[20] and experiment,[21] one can predict the perovskite-based catalyst activity to follow its electronic structure, which—in the case of the perovskite structure—can be conveniently controlled by a combination of A-site and B-site cations.[22] In fact, perovskite-based catalysts represent a rather popular structural type of catalysts in alkaline media.[16] The highest activity among perovskite-based OER catalysts has been predicted for LaNiO$_3$ as well as for Ba$_{0.5}$Sr$_{0.5}$Co$_{0.8}$Fe$_{0.2}$O$_3$, which both reside close to the top of the oxygen evolution activity volcano.[20,21] In particular, LaNiO$_3$ is considered a prospective candidate for optimization. Several reports[23−27] have shown that the synthetic route has a distinct influence on the morphology and electronic properties of lanthanum nickel oxide and consequently its activity in OER catalysis. Nanostructured LaNiO$_3$ particles of about 25 nm particle size were obtained using a freeze-drying technique and displayed very high OER activity if the particles were combined with a conductive carbon support.[28] The actual crystal structure found in various LaNiO$_3$ perovskites is also reported to significantly affect the OER activity. Directing the structure from rhombohedral to cubic is reported to improve the OER activity dramatically.[29] Strain effects have also been shown to influence the electrocatalytic properties of lanthanum nickel oxides.[30] The catalytic activity of lanthanum nickel perovskites can be further enhanced by introducing A-site vacancies affecting the overall redox properties of the material.[31] Substitution in the A-site[32,33] and B-site[34−36] of the perovskite structure was also reported to modulate the intrinsic catalytic activity of the material. Aside from the improvement of the catalyst's intrinsic activity, one may improve the feasibility of the catalyst by reducing its particle size[37−40] to increase the catalytically active surface area. Alternatively, one can also explore the surface sensitivity of the oxygen evolution reaction by exposing facets of higher intrinsic catalytic activity.[41−43] Ideally, in exfoliation, both approaches can be explored simultaneously.[44−47] It may be summarized that the optimization effects employed in the case of LaNiO$_3$ are based on the exploration of minor adjustments to the structure of the catalyst and/or on the maximization of the material's specific area without aspiring to

improve the intrinsic activity of the catalyst on an atomary level.

In this paper, we report on a novel rational approach of the OER activity optimization of catalysts based on Ni oxides. With LaNiO$_3$ perovskite as the initial material, structural variations are computationally introduced to maximize the presence of the trivalent Ni in the surface structure. The initial model catalyst and its structural modifications are then systematically investigated by DFT to identify structural motifs with improved OER activity. These theoretically predicted catalytically active motifs are then synthesized by a novel approach combining a template spray-freeze freeze-drying approach[48,49] followed by simple postsynthesis treatment. The experimental OER activity values are then compared with theoretical predictions.

■ RESULTS AND DISCUSSION

Structural Model Evaluations. Theoretical assessment of the OER activities of the new catalysts relies on a thermodynamic analysis based estimate of the limiting overpotential of the oxygen evolution reaction. This is based on an assumption that the entire oxygen-evolving process is a sequence of four-electron proton transfer steps.[20] These electron–proton transfer steps are summarized as follows:

$$H_2O + * \rightarrow OH* + H^+ + e^- \tag{1}$$

$$HO* \rightarrow O* + H^+ + e^- \tag{2}$$

$$H_2O + O* \rightarrow OOH* + H^+ + e^- \tag{3}$$

$$OOH* \rightarrow * + O_2 + H^+ + e^- \tag{4}$$

where the asterisk represents a binding site on the surface of the catalyst.

The scheme of the process depicted by eqs 1−4 is valid regardless of the pH and may also be used to rationalize the behavior of the systems designed for alkaline media such as, for example, LaNiO$_3$.[50,51] Oxygen may be evolved only if the overall reaction sequence is thermodynamically spontaneous, i.e. each of the reaction steps (1)−(4) is thermodynamically spontaneous. The step requiring the highest free energy to

become thermodynamically spontaneous becomes the potential-controlling step, and the free energy associated with it is used to calculate the theoretical overpotential.

It may be also devised that the surface-confined active site(s) responsible for oxygen evolution has to be redox-active (i.e., capable of changing its oxidation state). Hence, one may assume that in the case of LaNiO$_3$-based catalysts the oxygen-evolving activity is primarily attributable to Ni, its oxidation state, and its local environment. It needs to be noted that the whole concept of the oxidation state is not native for DFT; hence, its change needs to be introduced by a modification of the local structure. Assuming LaNiO$_3$ perovskite to be the initial well-defined structure (see Figure 1a), one can theoretically conceive a series of intermediate oxides derived from the perovskite LaNiO$_3$ containing a variable, yet decreased, amount of lanthanum near the surface (see Figure 1b,c).

The DFT-based energy optimization of the theoretically conceived structures depicted in Figure 1a–c suggests that the original perovskite arrangement features two types of metal–metal pairs[75] characterizing the surface structure; one relevant to pairs of neighboring Ni–Ni atoms at a distance of ca. 3.7 Å (solid arrow in Figure 1d) and the distance of neighboring Ni–La atoms (dotted arrow in Figure 1d) at a distance of ca. 3.3 Å. The perovskite structure responds to La removal in two principal ways: (i) by cationic rearrangement in the bulk of the structure and (ii) by structural adjustment connected with a formation of new La-free surface structures. Computational structure optimization predicts that the removal of La triggers a formation of Ni-enriched regions in the bulk where recombination of Ni atoms yields Ni pairs with an interatomic distance of ca. 3.5 Å (see arrows in Figure 1e). Recombination after the La leaching, however, also leads to the formation of a new surface where the surface reconstruction leads to a completely new arrangement of Ni with Ni–Ni pairs at a distance of ca. 2.85 Å (see dashed arrow in Figure 1f). The average oxidation state of Ni remains III, as follows from the average Ni–O distance of ca. 1.9 Å found in both proposed structural motifs, reflecting the La removal.

Regardless of whether these surface structures may actually exist, they may be computationally assessed toward their activity in the oxygen evolution process. The theoretical OER overpotentials of the surface structures depicted in Figure 1 were evaluated and compared with the generalized oxygen evolution volcano, as shown in Figure 2. The DFT results summarized in Figure 2 outline the striking difference between the behavior predicted for the stoichiometric LaNiO$_3$ and the surfaces created after La removal.

The La removal in principle forms either Ni-exposed or Ni-recombined surfaces, the catalytic behavior of which is fundamentally different from stoichiometric LaNiO$_3$. The theoretically conceived behavior of the La-depleted La$_x$NiO$_3$ material shows smaller deviations from the ideal catalyst behavior (with all charge transfer steps driven with the same free energy) than the stoichiometric LaNiO$_3$. As shown in the data presented in Figure 2, the newly created Ni exposed surface (blue marker in Figure 2) shows significantly higher intrinsic activity in comparison to the conventional LaNiO$_3$ perovskite surface.

In contrast to the Ni exposed surface (see Figure 1b,e), which features only one type of possible active site, the Ni recombined surface shows two types of available Ni surface sites. The reactivities of both available surface Ni sites (1 and
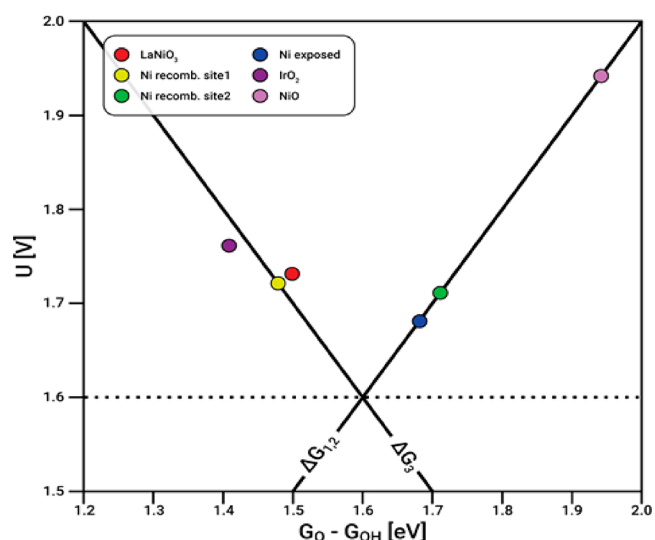

Figure 2. DFT-based activity volcano for the oxygen evolution reaction. The activity of the modified La-depleted surfaces is higher than that of the conventional stoichiometric surface.

2; see Figure 1c) differ significantly, even though both types of surface Ni sites yield a similar theoretical OER overpotential. It also needs to be noted that the descriptor used, a difference of G_O and G_{OH}, may be also taken as an approximation of the redox potential associated with oxidation/reduction to/from an active state in which the Ni stays in oxidation state III.

In this manner, one should expect the strongly binding Ni recombined site 1 to show a Ni(II) to Ni(III) transition in the interval 1.4–1.5 V. In contrast, the weakly binding Ni recombined site 2 ought to show the same transition above 1.7 V, coinciding with the oxygen evolution process.

While the Ni site 1 (see Figure 1c and yellow marker in Figure 2) can be easily oxidized and consequently resides on the strong binding branch of the volcano, the other available Ni surface site (site 2 in Figure 1c and green marker in Figure 2) shows greater resistance to the first electron transfer, which results in its position on the weak binding side of the OER volcano, making the binding of the *OH intermediate on the surface the potential-determining step. Such a difference in reactivity of both Ni surface sites is not surprising, given the proximity to the apex of the oxygen evolution volcano.

The activity of the recombined surface for both sites (site 1 (yellow marker) and site 2 (green marker); see Figure 2) is slightly lower than that of the Ni-exposed (i.e., non-recombined) surface (blue marker on the volcano), yet it remains closer to the apex of the volcano than the stoichiometric LaNiO$_3$. Although a thermodynamic analysis of the intrinsic OER activity for both types of La-depleted surfaces clearly favors the Ni exposed surface, the thermodynamic prediction does not automatically translate into superior practical activity of the Ni exposed surfaces. Given the thermodynamic nature of the analysis based on DFT calculations, the theoretical overpotentials are normalized per single active site. The predictions of practical OER activity, therefore, need to reflect the difference in densities of the active sites on the surface. In fact, the Ni recombined surface has a higher density of active sites per surface area in comparison with other theoretically conceived surface structures. In particular the density of sites of recombined Ni surface exceeds that of the Ni exposed surface by a factor close
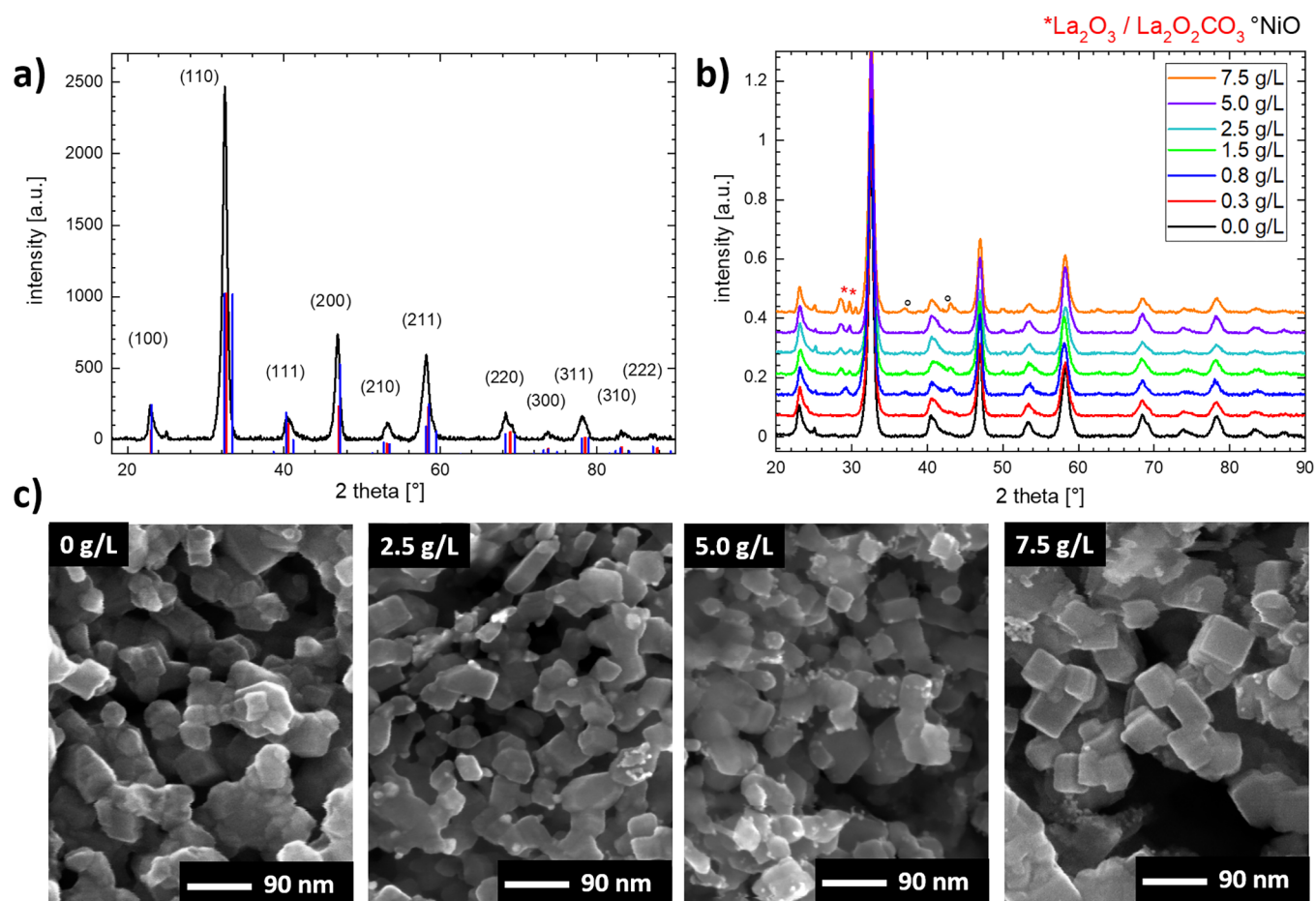
Figure 3. (a) Powder diffraction pattern of a lanthanum nickel oxide sample synthesized without added gelatin indexed with reference for cubic LaNiO$_3$ (red, $Pm\overline{3}m$, No. 221). For comparison the reference for rhombohedral LaNiO$_3$ (blue, $R3c$, No. 167) is added. (b) Powder diffraction patterns of lanthanum nickel perovskites synthesized with different amounts of gelatin. Peaks associated with lanthanum-based contaminations (La$_2$O$_3$/La$_2$O$_2$CO$_3$) are marked with asterisks (*) and NiO (°). (c) SEM micrographs of selected LaNiO$_3$ nanoparticles prepared with different gelatin concentrations.

to 2. This higher active site density effectively brings the practical activity of the Ni recombined surface up to the level of the Ni exposed surface, which is superior to that of conventional LaNiO$_3$.

The theoretical overpotential observed for the La-depleted La$_x$NiO$_3$ oxides is about 50 mV lower than that of stoichiometric LaNiO$_3$, which represents about an order of magnitude faster kinetics of the OER on La-depleted materials. The results of the DFT modeling conclusively show that the activity of LaNiO$_3$ perovskites in oxygen evolution can in principle be significantly improved if one stabilizes La-free perovskite-related surface structures and prepares them on real catalysts.

Material Synthesis. The synthesis of the structures theoretically identified as superior OER catalysts represents a significant challenge. Conventional synthetic approaches lead to the formation of stoichiometric LaNiO$_3$. In the case of the spray-freeze freeze-drying process[48,49] in the La-Ni system, an amorphous precursor is obtained, which needs to be crystallized at elevated temperatures. The ternary lanthanum nickel oxide is formed at calcination temperatures as low as 700 °C (see Figure 3a). The ternary lanthanum nickel oxide formed conforms to the perovskite structural type.

Detailed information on the structure of the prepared LaNiO$_3$ phases can be extracted from the Rietveld refinement

of the experimental XRD patterns (see Figure S1 in the Supporting Information). Although the ideal perovskite structure is cubic, the variation in the sizes of the cations occupying both available types of cationic positions may trigger tetragonal or orthorhombic distortions. It needs to be noted that the precise structural determination of the materials prepared in the spray-freeze freeze-drying approach is complicated by the nanoparticulate nature, which deteriorates the quality of the diffraction data due to the limited size of the coherent domains.

The refinement procedure of the experimental patterns gives the best convergence, assuming that the prepared materials conform to the rhombohedral perovskite structure ($R\overline{3}c$, No. 167): i.e., deviating from the ideal cubic perovskite (see Figure S1b).

A closer approach toward the theoretically predicted structures may be achieved by a combination of the spray-freeze freeze-drying synthesis in the presence of a structure-directing gelatin[52,53] followed by postsynthesis treatment. The synthesis in the presence of a structure-directing gelatin leads to a formation of nanocrystalline phases which are apparently identical with those synthesized in the absence of the structure-directing agent (see Figure 3b). The addition of a structure-directing gelatin eventually leads to the formation of secondary crystalline phases contaminating the produced materials. The
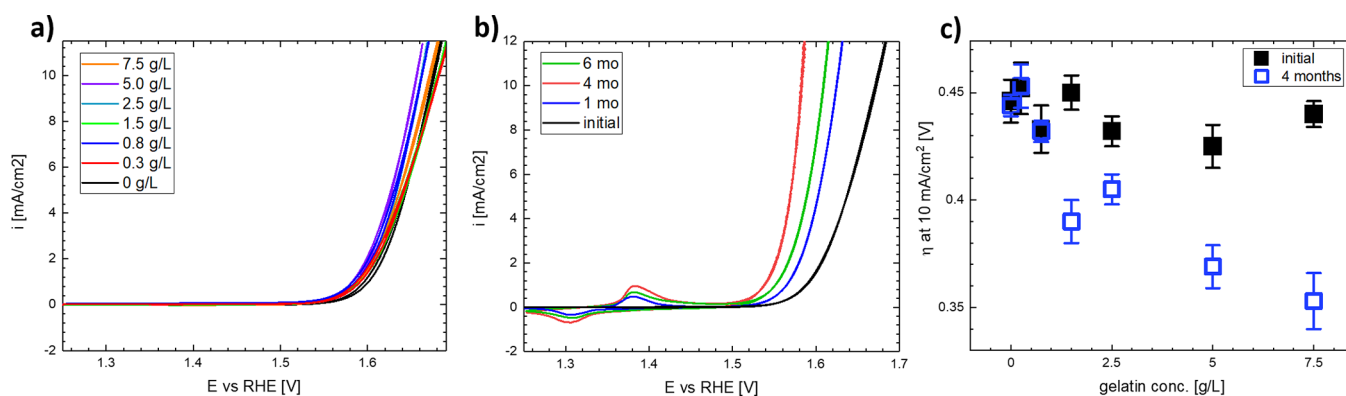
Figure 4. Cyclic voltammograms (CVs) of LaNiO$_3$ catalyst samples synthesized with varying amounts of gelatin, measured at 5 mV/s scan rate in 0.1 M KOH. The working electrode is the catalyst ink drop-cast onto GC-RDE support at 1600 rpm rotation rate. Initial CVs of all synthesized samples are given. (b) CVs of LaNiO$_3$ of the LaNiO$_3$ perovskite sample synthesized with a gelatin concentration of 7.5 g/L after different periods of ink aging. (b) Overpotential at a current density of 10 mA/cm as a function of gelatin for the initial samples (black) and after the postsynthesis ink aging for 4 months (blue).

diffraction signals of these secondary phases can be attributed to La-rich phases, most likely La$_2$O$_3$ or La$_2$O$_2$CO$_3$. The La-rich contaminating phases are accompanied by a small fraction of NiO to maintain the stoichiometry of the reaction mixture. The amount of these additional phases, however, remains below 5% (2% of NiO), and their effect on the catalytic behavior can be neglected. Details of the Rietveld analysis are given in Table S1 and Figure S2 in the Supporting Information.

The structure-directing gelatin has a pronounced effect on the morphology of the synthesized materials as well as on the local structure (see Figure 3c and Figure S3 in the Supporting Information). The LaNiO$_3$ materials prepared in the absence of gelatin show a random particle shape, indicating a random orientation of the surface. The addition of gelatin directs the nanoparticle growth toward prisms with a rhombohedral base and with increasing gelatin content also prisms with a rectangular or square-like base (see Figure 3c). The particle size analysis reveals very similar average particle sizes of around 35 nm for all of the samples, regardless of gelatin content (see details in Figure S4 in the Supporting Information).

Electrocatalytic Activity. The oxygen-evolving activity of the prepared phases is reflected in cyclic voltammograms of the prepared LaNiO$_3$ nanocrystalline catalysts recorded in 0.1 M KOH solution in the potential range of 1.2−1.7 V vs RHE (Figure 4). To facilitate the reader's orientation, we will further use the potential necessary to drive the current density of 10 mA/cm^2 (of the projected electrode area) as a benchmark characteristic depicting the activity of the prepared materials. As follows from Figure 4, there is no significant difference in the oxygen evolution activity, which may be attributed to the surface orientation effects associated with the presence of gelatin in the reaction mixture. All investigated materials show a comparable activity when the current density of 10 mA/cm^2 needs to be driven by overpotentials of 430−450 mV, which are comparable with those of materials prepared by sol−gel synthesis.[25]

However, a significant improvement in the catalytic activity is observed for catalysts prepared in the presence of gelatin if they are stored in the Nafion-containing ink (see Figure 4b). The oxygen-evolving activity of the electrodes based on such materials improves with the amount of gelatin (see Figure 4c) and with storage time. The general behavior can be

demonstrated on the sample of the material prepared in the presence of gelatin in a concentration of 7.5 g/L, where aging of the electrochemical ink leads to a significant decrease in the overpotential needed to drive the current density of 10 mA/cm^2 from its initial value of 442 mV to 395 mV after 1 month and to 353 mV after 4 months (Figure 4b). Such an overpotential is comparable to that of state of the art perovskite OER catalysts in alkaline media: e.g., hexagonal BSCF with $\eta \approx 340$ mV.[54] Further storage of the catalyst, however, leads to a pronounced drop in the oxygen-evolving activity (6 months, green curve in Figure 4b). The aging-related increase of the catalyst activity might be in principle attributable to variations in catalysts loading due to a change of the ink concentration during the aging process. Such an explanation, however, cannot be accepted, since the aging of the ink leads to a significant structural development of the catalyst (see below). The observed behavior cannot be qualified using the XRD-based structure and prompts more detailed structural characterization on a local level based on HRTEM and XAS.

Aside from the significant increase in OER activity, one also finds a distinct redox feature characteristic for the Ni^{II}/Ni^{III} redox couple in voltammograms based on materials prepared in the presence of gelatin. This Ni^{II} to Ni^{III} transition is not observed in electrodes made from freshly prepared inks. It also needs to be noted that the signal attributable to a Ni^{II} → Ni^{III} transition is absent in the first anodic scan on a pristine electrode. This suggests that the electrodes originally do not contain any oxidizable Ni^{II}, which forms only in situ during the cathodic scan of the voltammetric experiment. The intensity of the Ni^{II}/Ni^{III} redox increases both with aging and, in general, also with the content of gelatin used in the synthesis. The intensity of the Ni^{II}/Ni^{III} redox feature yields a reasonable correlation with the measured activity (see Figure S5 in the Supporting Information).

It needs to be noted that the presence of the Ni(II) to Ni(III) transition at potentials slightly below 1.4 V vs RHE shows a reasonable agreement with the theoretically conceived reactivity of the strongly binding (site 1) Ni on the recombined surface presented in Figure 2. The observed experimental trend, when the resolved Ni^{II} to Ni^{III} transition signal increases with aging, is attributable to the increasing presence of the reconstructed Ni site at the surface. Since it is
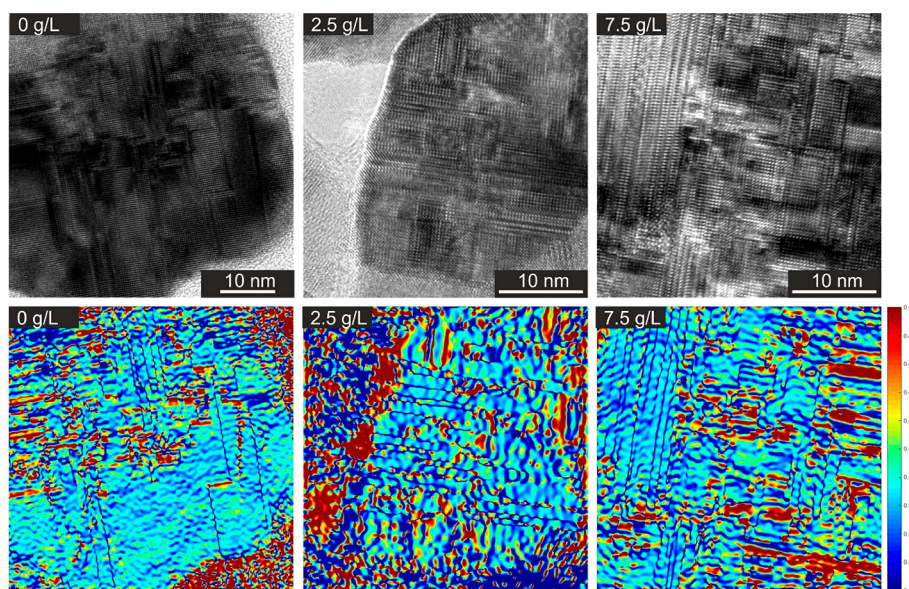
Figure 5. HR-TEM micrographs of selected LaNiO$_3$ nanoparticles with varying gelatin concentrations. The respective concentrations are given in the picture insets. Corresponding maps of *d*-spacing variation calculated by GPA are shown to outline the domain structure of the materials prepared in the presence of gelatin.
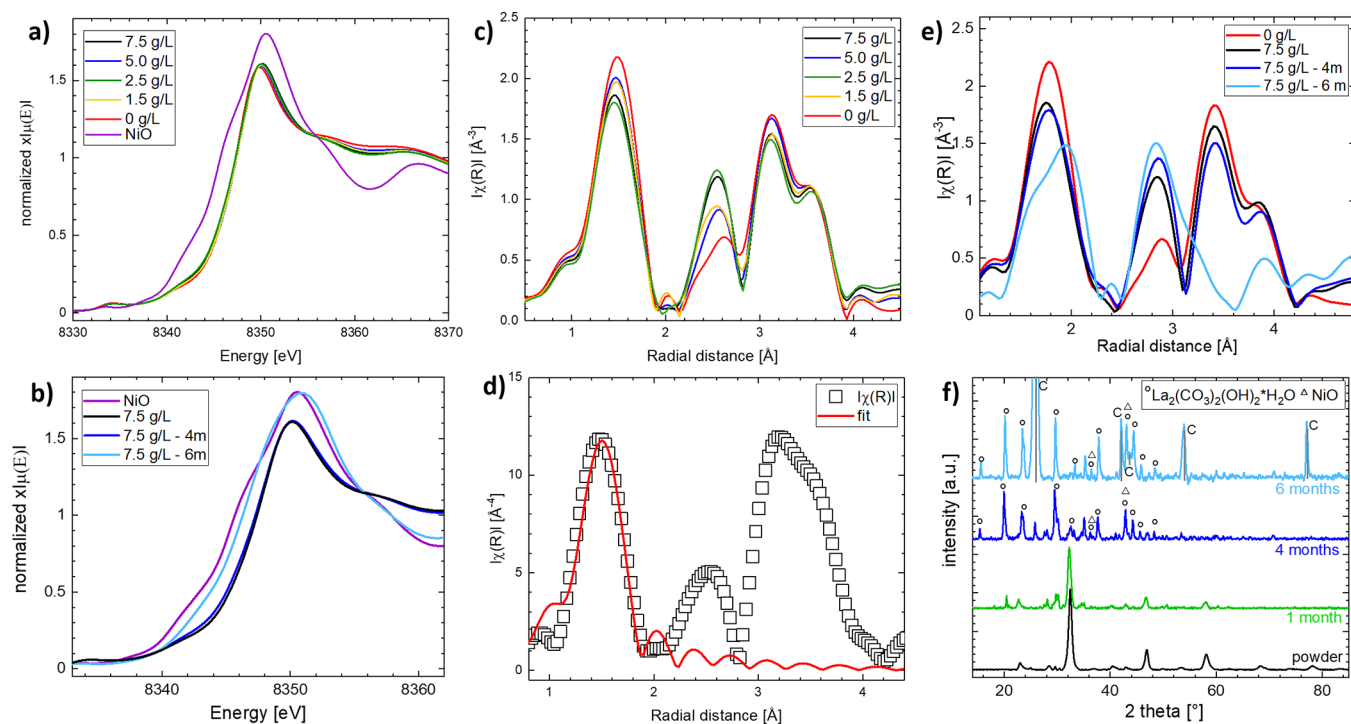

Figure 6. XANES spectra (a) of the synthesized lanthanum nickel oxide powder samples and (b) of the 7.5 g/L sample aged for different amounts of time (4 months, blue; 6 months, light blue), including the initial powder sample (black), measured at the Ni K-edge. The XANES spectrum of NiO is included as a reference. (c) Fourier transformed EXAFS functions in *R* space of the initial powder samples, weighted with k^2, measured at the Ni K-edge, depicted without phase correction. (d) Typical NLLS fit (red line) of the theoretical model using a one-shell model of LaNiO$_3$ rhombohedral perovskite and NiOOH in a fitting range from 1.1 to 2 Å in *R* space for the EXAFS function of the sample with 1.5 g/L gelatin concentration (□) normalized with k^3. (e) Fourier-transformed EXAFS functions in *R* space of the 7.5 g/L sample aged for different amounts of times, weighted with k^2, measured at the Ni K-edge, depicted with applied phase correction. The 7.5 and 0 g/L initial powder samples are included for comparison. (f) XRD patterns of the LaNiO$_3$ sample prepared with 7.5 g/L gelatin collected after different ink aging times. The 6-month-old sample was prepared on graphite; the reflections that originate from the graphite substrate are marked in gray and indicated by C.

visible that the Ni^{II}/Ni^{III} redox charge correlates with increased activity, one may attribute the OER activity of the prepared materials to the strong binding sites of the Ni reconstructed active sites.

Local Structure Characterization. *HR-TEM.* High-resolution transmission electron microscopy (HR-TEM) data (see Figure 5) show that all samples are composed of cuboid particles composed of rhombohedral LaNiO$_3$. The particles

contain twinning domains compensating for the lower rhombohedral symmetry. The addition of gelatin leads to a decrease in the domain size and, therefore, an increase of the surface of domain boundaries. The formation of similar stacking faults has been reported previously in La-Ni-O materials.[55,56] On the twinning boundaries, the formation of Ruddelsden−Popper (RP) faults, when the stacking of NiO and LaO layers in the structure is broken and double LaO layers are formed, can be expected.[55,56] It needs to be stressed that the formation of RP faults leads to a shift in the stacking of the layers and causes a separation of La and Ni on a subnanometer scale. The presence of the stacking faults is visualized in Figure 5 by an analysis of the d-spacing variance, which clearly distinguishes the density of the faults at the boundaries of the coherent domains that increases with increasing gelatin concentration.

However, this separation is confined mostly to the bulk of the material and should not have an immediate effect on catalytic behavior, as reflected in Figure 4a. A more detailed analysis of the HR-TEM data also yields additional structural information on the material phase composition, confirming the presence of additional phases, identified also in XRD patterns. A detailed analysis of the local phase analysis is given in Figure S6 in the Supporting Information.

X-ray Absorption Spectroscopy. The X-ray absorption near edge structure (XANES) spectra of the Ni K-edge in prepared $LaNiO_3$ powders are shown in Figure 6a.

The absorption edge position of the lanthanum nickel samples appears at ca. 8348 eV, which is about 3 eV higher than that of the NiO reference (8345 eV). The Ni edge position obtained in $LaNiO_3$ is compatible with the projected oxidation state of Ni^{III}.[57] The same oxidation state of Ni is also observed in catalysts subjected to aging in Nafion-containing inks for less than 4 months (see blue curve in Figure 6b and Figure S7 in the Supporting Information). A longer aging of the catalysts, however, leads to a gradual decrease in the oxidation state of Ni (see light blue curve in Figure 6b). The XANES-based oxidation state of Ni is further corroborated by the average Ni−O bond length, which remains close to 1.9 Å for all samples aged for less than 6 months. The lowered oxidation state of Ni suggested for materials aged for 6 months is matched by an elongation of the Ni−O distance, which climbs above 2 Å for this material.

Since the high oxidation state of Ni is retained in all catalysts save for those aged in Nafion-containing ink for more than 4 months, regardless of the different synthesis or aging conditions, one needs to seek additional structure-related information to qualify the observed changes in the oxygen-evolving activity of the prepared catalysts. This additional information can be extracted from the EXAFS-based Ni local environment structure, which shows significant variability for different $LaNiO_3$ samples (see Figure 6c). Three distinct signals located at ca. 1.8, 2.8, and ca. 3.4 Å are identified in the Ni K EXAFS functions . Assuming a rhombohedral perovskite structural model, one may expect the signal located at ca. 1.8 Å to reflect the direct Ni−O scattering in the first coordination shell. The pronounced signal located at ca. 3.4 Å can then be attributed to the cation−cation interaction between Ni in the B-site and La located in the A-site of the perovskite structure. A relatively weak scattering signal, located near 2.8 Å, can be attributed to indirect scattering involving two of the Ni coordinating oxygens. This structural model works well for the Ni K-edge EXAFS functions of the $LaNiO_3$ prepared in the

absence of gelatin (see Figure S8 in the Supporting Information) but fails for the $LaNiO_3$ materials prepared in the presence of gelatin: namely, in the region near 2.8 Å.

The relative intensity of the feature located at 2.8 Å increases with increasing gelatin content and shows a different sensitivity to k normalization than in the case of $LaNiO_3$ prepared without gelatin (see Figure S9 in the Supporting Information). The observed behavior suggests that the signal located at 2.8 Å in the materials prepared with gelatin also integrates a metal−metal scattering interaction. The contribution from this metal−metal scattering increases with increasing gelatin content. The increase in this metal−metal scattering is also accompanied by a decrease in the intensity of signals attributable to Ni−O scattering (ca. 1.8 Å) and Ni−La scattering (ca. 3.4 Å) (see Figure 6c).

Such a signal is typical for nickel−nickel arrangements typical for NiO[58] or other nickel oxo compounds such as NiOOH.[59,60] It may be, therefore, assumed that the Ni present in the materials prepared in the presence of gelatin exists in two local arrangements, one resembling a La-abated NiOOH-like environment (which introduces metal−metal scattering at ca. 2.8 Å), and one having a perovskite local environment (introducing Ni-La scattering at 3.4 Å). One may deconvolute the local structure data assuming the coexistence of these two local environments. The content of each Ni local environment was estimated from a first-shell EXAFS function refinement (see Figure 6d) under the constraint that the Ni−O bonding distance and coordination number of Ni for both local environments remain constant ($r(Ni−O)_{NiOOH} = 1.91$ Å and $r(Ni−O)_{LaNiO_3} = 1.93$ Å, respectively).

The fraction of the nickel-rich NiOOH-like environment increases with increasing gelatin content (see Table S2 in the Supporting Information). This trend is in agreement with the growing number of RP faults observed in HRTEM. It needs to be further stressed that the EXAFS-based local structure analysis describes the situation in the materials' bulk and, as shown by the data presented in Figure 4a, variations of the Ni local arrangement attributable to the gelatin content have no immediate effect on the electrocatalytic activity. The aging of the $LaNiO_3$ catalysts in the Nafion-based inks for up to 4 months has no qualitative effect on the Ni local structure of the prepared catalysts (see blue curve in Figure 6e and Figure S10 in the Supporting Information). The only discernible effect one observes is a slight increase in the presence of Ni in a NiOOH-like environment.

The local structure, however, qualitatively changes for longer aging times (see light blue curve in Figure 6e) when the observed Ni EXAFS functions fail to show any scattering characteristic for La−Ni pairings with a distance of ca. 3.4 Å. The suppression of the signal characteristic for the perovskite environment is partially compensated by an increase in the metal−metal scattering with a distance of ca. 2.8 Å, characteristic for NiO or NiOOH.

This local structure development is complemented by a pronounced shift of the Ni absorption edge to lower energies (cf. Figure 6b), which identifies the local environment of Ni as that typical for cubic NiO. The NiO structural model works well for the Ni K-edge EXAFS functions of 6 month aged inks (see Figure S11 in the Supporting Information).

The local structure development of the aged $LaNiO_3$ catalysts is also indirectly reflected in the pronounced development of the diffraction patterns of the aged $LaNiO_3$
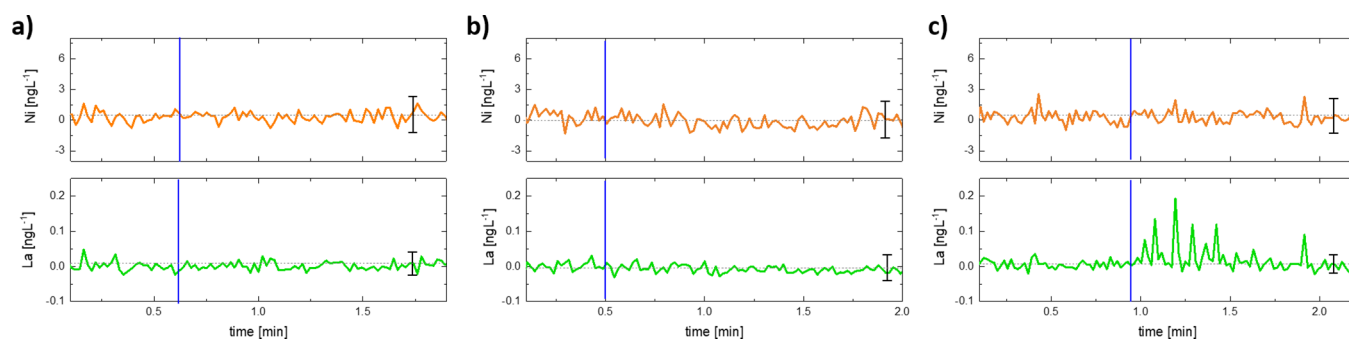
Figure 7. ICP-OES signals of lanthanum and nickel present in the 0.1 M KOH electrolyte with no applied potential for (a) a freshly prepared ink with a gelatin concentration of 5.0 g/L, (b) an aged ink synthesized without the addition of gelatin, and (c) an aged ink with a gelatin concentration of 5.0 g/L. The contact time of the electrode with the electrolyte solution is indicated by the blue vertical line. The detection limit is marked for each experiment as the black error bar.

materials (see Figure 6f). As shown by the patterns presented in Figure 6f, the aging of the LaNiO$_3$ materials in Nafion-based inks leads to the apparent destruction of the LaNiO$_3$ perovskite nanocrystals. The reflections typical for rhombohedral LaNiO$_3$ decreases in intensity with time and cannot practically be identified in the patterns of the materials aged for more than 4 months. The observed XRD patterns become dominated by La-containing phases, namely by La$_2$(CO$_3$)$_2$(OH)$_2$·H$_2$O (PDF #00-046-0368). The observed diffraction patterns are further complemented with small contributions from NiO (the reflections of which, unfortunately, overlap with those of lanthanum carbonate) and additional lanthanum phases such as LaO and La$_2$O$_3$ (see Figure S12 in the Supporting Information).

Combining the structural information on the basis of both XRD and EXAFS data with the local arrangement information provided by HRTEM, one may conclude that the observed significant improvement in the OER activity is facilitated by the specific action of the local structure-forming gelatin. It may be also concluded that this effect is confined to a length scale inaccessible by conventional X-ray diffraction. Comparing the local structure of the LaNiO$_3$ prepared in both the presence and absence of gelatin, one may propose that the gelatin, in fact, controls the distribution of the stress/strain connected with the A-site and B-site cation size in the LaNiO$_3$ perovskite. The materials prepared in the absence of gelatin use the high entropy of the randomly oriented surface to release the stress/strain. The materials prepared in the presence of the gelatin, which show a high degree of faceting and a relatively high orientation of the surface, locate the same stress/strain in the RP faults in the nanocrystal bulk. In fact, the RP faults facilitate exposing the Ni-rich structural motifs reflected in the EXAFS data (Ni−Ni scattering distance of 2.8 Å) to the surface. This may be achieved by selective leaching of the La confined in the RP stacking faults. Such a process is compatible with the identified formation of La$_2$(CO$_3$)$_2$(OH)$_2$·H$_2$O in the aged materials. The formed nanometer to subnanometer perovskite-like domains are not reflected in the XRD patterns due to the limited ability of the conventional diffraction techniques to address structural features on the nanometer or subnanometer length scale. This mechanism is further confirmed by selective removal of the perovskite stabilizing La, which can be followed by ICP-OES experiments (see Figure 7). The La leaching is recorded in ICP-OES experiments, which clearly detect a transfer of La in the solution upon contact of the aged materials with the electrolyte solution (see Figure 7).

As follows from the ICP-OES data, contact with the electrolyte (0.1 M KOH) does not trigger any visible leaching from the freshly prepared LaNiO$_3$ ink samples (Figure 7a). The same behavior is also observed for materials prepared without gelatin (Figure 7b). Electrodes based on aged inks of catalysts prepared with gelatin, however, release lanthanum into solution immediately upon contact with the electrolyte solution (see Figure 7c). It needs to be noted that the signal of solution-based La in these experiments is rather discontinuous, which suggests lanthanum leaching from confined regions rather than from the entire bulk of the ternary phase. This leaching is facilitated by the presence of Nafion in the catalyst. The process, therefore, likely involves an increase in the overall surface area and can be viewed as an analogue of an exfoliation. It needs to be noted that materials of similar structure indeed can be exfoliated in acid media.[61] Similarly, it is known that immersion of Nafion in aqueous solutions leads to a drop of the solution pH by up to 2 pH units.[62] In this context we may reasonably expect that the Nafion, aside from creating a mildly acidic environment, also facilitates stabilization of the exfoliated surface by preventing clustering and reassembly.[63] The improvement in the oxygen-evolving activity by aging is connected with creating acid conditions (attributable to the sulfonic groups of the Nafion) and cannot be achieved with another polymeric binder (see Figure S13 in the Supporting Information). The oxygen evolution activity improvement then becomes proportional to the density of the RP faults in the prepared LaNiO$_3$ nanocrystals and becomes apparent only for materials prepared with a significant gelatin concentration (>1.5 g/L) (cf. Figure 4c and Figure S14 in the Supporting Information). This suggests that that the observed behavior could be related to the Ni environment with a Ni−Ni pairing at 2.8 Å and its eventual exposure on the material's surface.

The observed improvement in the oxygen-evolving activity of the Nafion aged materials is significant and apparently confirms the theoretical prediction presented in Figure 4). This agreement, however, needs to be taken with care, as the experimental data can be described by an alternative interpretation. One needs to bear in mind that the aging of the catalysts causes an increase in the surface area, the effect of which may possibly overlap with the effect of the theoretically predicted intrinsic activity improvement. The quantitative effect of the electrode surface area, however, does not play a dominant role, as can be deduced from the fact that the catalysts lose their activity immediately once the oxidation state of Ni starts to drop below III (cf. Figure 4b). In addition,

the qualitative nature of the observed OER activity improvement is reflected also in the observed change of the Tafel slope (see Table 1). It should be stressed that the Tafel slope

Table 1. Slopes Derived from the Tafel Lines of the Oxygen Evolution on Perovskite Catalysts Measured for Initially Prepared Catalyst Suspensions and after 4 Months of Aging of the Ink Suspensions, Extracted from Steady-State Chronoamperometric Measurements in 0.1 M KOH

gelatin concn (g/L)	initial (mV/dec)	4 months (mV/dec)
0	65 ± 2	66 ± 3
1.5	55 ± 3	51 ± 2
2.5	57 ± 1	46 ± 4
5.0	52 ± 3	43 ± 4
7.5	52 ± 1	43 ± 1

remains aging insensitive in the case of materials prepared without gelatin. On the other hand, the Tafel slope changes from ca. 55 mV/decade to ca. 40 mV/decade upon aging in Nafion-containing ink (see Table 1). This trend reflects a change in the mechanism of the whole OER process and suggests a change of the kinetic control to the third electron transfer caused by aging. The significant difference between the Tafel slope of the $LaNiO_3$ prepared without gelatin and those of the aged $LaNiO_3$ synthesized in the presence of gelatin also reflects the effect of the surface orientation, which is quite heterogeneous for the materials prepared without gelatin. The random surface orientation explains in this case the rather high Tafel slope value observed experimentally (60 mV/decade), which deviates from the fact that the DFT prediction (based on a (100) surface orientation) of the third electron transfer being the potential-controlling step (which should result in a Tafel slope of close to 40 mV/decade).

The theoretical prediction of the third electron transfer to be the potential-limiting step on the first type of the active site on the reconstructed surface (see Figure 2) seems to be, on the other hand, confirmed in the experimental values observed for aged electrodes based on $LaNiO_3$ prepared in the presence of gelatin. It also needs to be noted that the theoretical prediction assumes that the activity improvement requires the Ni to reside in the perovskite-like local environment. This implies that the complete leaching of La from the structure we apparently encounter in the samples aged for 6 months should inevitably lead to a drop in the OER activity. This drop in the OER activity is indeed observed and is also accompanied by an increase in the Tafel slope to ca. 60 mV/decade. The complex variations of the Tafel slope are difficult to explain and suggest that the catalytically active sites are in fact formed only under operando conditions. The prepared materials and their available structural information, therefore, describe just a precursory state and further in situ XAS experiments would be needed to fully qualify the difference of the active sites formed on individual materials.

The observed OER activity data, nevertheless, confirm the theoretical prediction of the superior activity of La-depleted surface layers. It needs to be noted, however, that the observed change in oxygen-evolving activity is higher than that predicted theoretically for the La depletion of $LaNiO_3$. This behavior is not surprising, since the theoretical prediction of higher activity is based solely on intrinsic activity and/or crystallographic active site density. It remains insensitive to possible

changes in the specific surface area caused by chemical processes such as dissolution and exfoliation (see above).

As-prepared and exfoliated $LaNiO_3$ related oxides are reasonably stable under operando conditions, as shown by ICP-OES experiments (see Figure S15 in the Supporting Information), and the catalysts seem to be stable up to a potential of 1.9 V vs RHE. Exposure of the electrodes to higher potentials results in an increase in coinciding signals of La and Ni in the solution. This behavior indicates a disintegration of the electrodes when the whole particles are loosened from the electrode due to vigorous bubble formation rather than selective leaching of any component from the catalyst under operando conditions.

CONCLUSIONS

The rational design principle in electrocatalysis conventionally comprises the DFT screening of thermodynamically stable phases as prospective catalysts. The data shown on the $LaNiO_3$ optimization, however, represent a qualitative improvement of this approach, since they describe a combined theoretical and experimental approach toward the exploration of metastable phases which, on the basis of theoretical analysis, have the potential to outperform materials populating the apex of the oxygen evolution volcano curve.

The spray-freeze freeze-drying approach in the presence of gelatin as a structure-directing agent demonstrates the potential to prepare and activate the phases conceived theoretically (i.e., without a support in existing structures) as materials with superior OER activity. The control obtained with the structure-directing gelatin allows the preparation of materials with identical XRD diffraction patterns differing significantly, however, on the local level. High-resolution transmission electron microscopy and X-ray absorption spectroscopy apparently identify a separation of La and Ni on the subnanometer level in the phases prepared: namely, if the synthesis of the materials was done in the presence of gelatin. This defect local structure can be viewed as Ni-enriched regions separated by La-rich Ruddelsden−Popper (RP) faults. The formation of these RP faults triggers cation redistribution in the Ni-rich domains, leading to the arrangements predicted by DFT.

The Ni-rich regions contain Ni solely in the oxidation state III and are capable of significantly improving the OER activity of the prepared materials if they are exfoliated to the surface. It needs to be stressed, however, that although maintaining the Ni in a high oxidation state is necessary to retain high OER activity, the actual observed activity improvement needs to be supported by a specific surface reorganization which enables— in agreement with the theoretical prediction—involvement of the strong binding active sites in the controlling step of the process. The observed drop in the overpotential needed to drive the OER at a current density of 10 mA/cm² is as much as 80 mV, from 440 mV to 360 mV. The gelatin also directs the morphology of the prepared $LaNiO_3$ nanocrystals toward prismatic crystals with a rhombohedral and (if the concentration of gelatin increases) rectangular or square base; however, this morphology direction shows no effect on the oxygen-evolving activity of the prepared materials. The observed activity is comparable with that reported for the most active OER catalysts for oxygen evolution.

■ METHODS

Density Functional Theory. The LaNiO$_3$ structures were optimized from the bulk using density functional theory (DFT) calculations with the use of the grid-based projector augmented wave (GPAW)[64,65] with the atomic simulation environment (ASE)[66] interface. The trigonal configuration of the perovskite unit cell ($R\bar{3}c$, No. 167) was used for the initial structure. Spin-polarized calculations were performed with a plane wave energy cutoff of 850 eV and a (10, 10, 10) k-point mesh. The PBE[67] functional to describe the exchange and correlation effects was used to optimize the bulk structure. (100) LaNiO$_3$ surfaces were created from the optimized bulk structure. The generalized gradient approximation (GGA) was used by implementing the BEEF-vdW[68] functional to express the exchange and correlation, with a grid spacing of $h = 0.20$ Å. All of the surface calculations were spin-polarized, the Brillouin zone was sampled with a k-point mesh of (4, 4, 1), and the atomic positions were relaxed until the total forces were lower than 0.08 eV/Å.

Synthesis. Lanthanum acetate hydrate (La(OOCCH$_3$)·H$_2$O, Sigma-Aldrich, 99.9%), and nickel lactate tetrahydrate (98%, Alfa Aesar) were used as the metal precursor salts. The crystal water content x of the lanthanum acetate was thermally analyzed using a SetSys Evolution system (Setaram) coupled with a quadrupole mass spectrometer (QMG 700, Pfeiffer). The lanthanum acetate was heated in an open alumina crucible under an argon stream (60 mL min^{-1}) in a temperature range of 30−1000 °C at a rate of 10 °C min^{-1}. The evolved gases were analyzed in multiple-ion detection mode (MID) when the intensity of individually selected fragments (mass to charge ratio) m/z = 12, 16, 17, 18, 28, and 44 was followed as a function of temperature. The crystal water content was found to be $x = 1.3$.

The LaNiO$_3$ samples were synthesized by the spray-freeze freeze-drying method.[48,49,69] The precursor solutions of lanthanum acetate and nickel lactate were prepared by dissolving the corresponding metal salts (ratio 1:1) as well as the respective gelatin amount (from 30 to 750 mg) in 100 mL of Milli-Q-quality deionized water. The total metal concentration was kept at 10 mM in all syntheses. The solutions were heated to 80 °C to allow the dissolution of the gelatin, stirred for 30 min, and left to cool off before the spray-freezing step. The ice-based precursor was prepared by spraying the starting solution into ca. 2 L of liquid nitrogen. The frozen solvent was removed in the freeze-drying step at reduced pressure (1 Pa) by employing a FreeZone Triad Freeze-Dry System 7400030 (Labconco). The following temperature protocol was employed in the procedure: −30 °C during the evacuation of the cooling chamber, followed by a gradual temperature increase (−30 °C (2 h), −25 °C (5 h), −20 °C (4 h), −15 °C (6 h), +30 °C (4 h)). The dry, foamlike precursor was carefully removed from the freeze-dryer and annealed at 700 °C for 2 h in a tube furnace in air.

The crystallinity and phase purity of the synthesized materials were analyzed using powder X-ray diffraction (XRD). The diffraction patterns were recorded using a Rigaku Miniflex 600 powder X-ray diffractometer with Cu Kα radiation operating at 30 kV and 10 mA. Ten scans were averaged to obtain the data quality needed for Rietveld analysis. Rietveld refinements were performed to determine the unit cell parameter as well as contamination content with the Profex 3.13.0 software package.[70] The morphology and particle

size of the prepared samples were analyzed using a Hitachi S4800 scanning electron microscope (SEM) equipped with a Nanotrace EDX detector (Thermo Electron). Transmission electron microscopy (TEM) was used to determine the defect nature of the prepared nanocrystals and was carried out on an FEI Tecnai TF20 X-twin microscope operated at 200 kV (FEG, 1.9 Å point resolution) with an EDAX energy dispersive X-ray (EDX) detector attached. Images were recorded on a Gatan CCD camera with a resolution of 2048 × 2048 pixels using the Digital Micrograph software package. High-resolution TEM (HR-TEM) micrographs were treated by geometrical phase analysis (GPA)[71] performed by CrysTBox.[72] The powder samples were dispersed in isopropyl alcohol, and the suspension was treated with ultrasonication for 5 min. A drop of the diluted suspension was placed on a holey-carbon-coated copper grid and allowed to dry by evaporation at ambient temperature.

X-ray Absorption Spectroscopy. Ni K-edge and La L$_{III}$-edge X-ray absorption spectra (XAS) of all samples were collected at the Inner-Shell Spectroscopy (ISS 8-ID) of the National Synchrotron Light Source (NSLS) II, Brookhaven National Laboratory. The incident beam was monochromated using a Si(111) cryogenically cooled double-crystal monochromator. Spectra were measured in fluorescence mode using a passivated implanted planar silicon (PIPS) diode detector. The absorption spectra were collected at room temperature and ambient pressure. The X-ray absorption spectra of the freshly prepared materials were measured on BN-based pellets (150 mg) containing 5−10 mg of the respective catalysts. Characterization of the catalysts relevant to their electrode-related behavior was performed on thin films prepared on rigid graphite carbon foil (0.125 mm, 99.95%, Good Fellow) substrates by drop-casting the catalyst inks (see below) to deposit a sufficient amount of catalyst (ca. 1−3 mg) on the substrate. Spectra were measured in an energy range of 8150−9150 eV at the Ni K-edge and 5300−5800 eV at the La L$_{III}$-edge. The absorption edge energies of the perovskite materials were determined from the X-ray absorption near edge structure (XANES) part of the collected spectra, using the maximum of the first derivative of the edge region. Extended X-ray absorption fine structure (EXAFS) data were analyzed using the Demeter program package based on the IFEFFIT libraries,[73,74] which included energy calibration, background subtraction, and edge step normalization. For the fitting, the $\chi(k)$ functions were weighted with k^2. The local structure parameters were refined from EXAFS functions by nonlinear least-squares (NLLS) fitting in the R space in the range of 1.1−2 Å. Details of the refinement (k range, goodness of fit (R factor), Debye−Waller factors σ, absorption edges E_0, occupation, and refined values of the effective scattering paths) are given in the respective tables.

Electrochemical Characterization. The activity of the prepared materials in the oxygen evolution reaction was evaluated from linear sweep voltammograms recorded in alkaline media. A standard single-compartment three-electrode cell was used in all experiments with an Analytics Rotator AFMSRXE RDE setup of Pine Instruments controlled by an Autolab PGSTAT30 apparatus. Thin-film catalyst layers deposited on glassy-carbon RDE supports were used as the working electrodes. A platinum mesh was used as the counter electrode and a saturated calomel electrode (SCE) as the reference electrode. All potentials were recalculated and are reported on the reversible hydrogen electrode (RHE) scale.

The catalyst ink suspensions were prepared using 10 mg of perovskite catalyst, 1.0 mL of Milli-Q-quality H_2O, 4.0 mL of isopropyl alcohol (≥99.5%, Sigma-Aldrich), and 20 μL of 5 wt % Nafion solution (Nafion 117, Sigma-Aldrich). The ink suspensions were sonicated for 30 min before depositing 10.0 μL on a polished glassy-carbon disk electrode (0.196 cm^2) to reach a total catalyst loading of 100 $\mu g\ cm^{-2}$.

The 0.1 M KOH electrolyte was prepared from KOH pellets (p.a., Lachema) by diluting with Milli-Q H_2O. Cyclic voltammograms were recorded at 5 mV s^{-1} in the potential range of 1.1−1.7 V. Tafel lines were derived from steady-state chronoamperometric measurements, in which the potential was gradually stepped from 1.2 to 1.6 V while it was held for 1 min at each potential. All measurements were corrected for uncompensated resistance of the system. Electrochemical impedance spectroscopy measurements were recorded in the range from 15 kHz to 1 Hz with an amplitude of 10 mV (peak to peak) to determine the ohmic resistance of the system. The presented current densities are based on the geometric surface area of the glassy carbon disk electrode.

In-Operando ICP-OES. Electrode dissolution was monitored during electrochemical experiments using a v-channel electrochemical flow cell (0.636 cm^2) connected to an Agilent 5100 ICP-OES spectrometer by direct injection. The ICP-OES signals of lanthanum (379.477 nm) and nickel (352.453 nm) in 0.1 M KOH diluted from a 38 wt % stock solution (VWR) were monitored as a function of time. Standard calibration curves were constructed from 0, 0.1, 0.2, 0.4, 0.6, 0.8, and 1.0 ppm (nickel) and 0, 0.13, 0.28, 0.55, 0.83, 1.1, and 1.4 ppm (lanthanum). The detection limit was estimated by calculating 3 times the standard deviation of the blank. The flow rate set by the peristaltic pump that supplied the ICP-OES was 1.5 mL min^{-1} for all experiments. Glassy-arbon plates of 2 mm thickness (Alfa Aesar) were used as catalyst substrates. The in-operando setup of the electrochemical cell combined with an ICP-OES spectrometer allows analyzing the stability of catalyst particles under an applied OER potential. The aged ink with 5.0 g/L gelatin concentration was chosen as a representative example. The potential was stepped from 1.4 to 2.0 V vs RHE in 0.1 V increments, with each potential step being held for 5 min.

ASSOCIATED CONTENT

ⓈI Supporting Information

The Supporting Information is available free of charge at https://pubs.acs.org/doi/10.1021/acscatal.0c04733.

> Details of the Rietveld refinement, SEM micrographs, histograms of the statistical particle size analysis, SAED, R space representations of EXAFS functions, and cyclic voltammograms (PDF)

AUTHOR INFORMATION

Corresponding Author

    Petr Krtil − *J. Heyrovský Institute of Physical Chemistry, Academy of Sciences of the Czech Republic, Prague 18223, Czech Republic;* ⓞ orcid.org/0000-0001-8447-1333; Email: Petr.Krtil@jh-inst.cas.cz

Authors

    Rebecca Pittkowski − *J. Heyrovský Institute of Physical Chemistry, Academy of Sciences of the Czech Republic, Prague 18223, Czech Republic*

    Spyridon Divanis − *Department of Chemistry, Copenhagen University, DK-2100 København, Denmark*

    Mariana Klementová − *Institute of Physics, Academy of Sciences of the Czech Republic, 182 21 Prague, Czech Republic*

    Roman Nebel − *J. Heyrovský Institute of Physical Chemistry, Academy of Sciences of the Czech Republic, Prague 18223, Czech Republic*

    Shahin Nikman − *Department of Chemistry, Lancaster University, Lancaster, U.K.*

    Harry Hoster − *Department of Chemistry, Lancaster University, Lancaster, U.K.;* ⓞ orcid.org/0000-0001-6379-5275

    Sanjeev Mukerjee − *Department of Chemistry and Chemical Biology, Northeastern University, Boston, Massachusetts, United States;* ⓞ orcid.org/0000-0002-2980-7655

    Jan Rossmeisl − *Department of Chemistry, Copenhagen University, DK-2100 København, Denmark;* ⓞ orcid.org/0000-0001-7749-6567

Complete contact information is available at:
https://pubs.acs.org/10.1021/acscatal.0c04733

Author Contributions

All authors have given approval to the final version of the manuscript.

Notes

The authors declare no competing financial interest.

ACKNOWLEDGMENTS

REFERENCES

(1) Fuel Cells and Hydrogen 2 Joint Undertaking. *Hydrogen Roadmap Europe: A Sustainable Pathway for the European Energy Transition*; Publications Office of the European Union: Luxembourg, 2019.

(2) Glenk, G.; Reichelstein, S Economics of converting renewable power to hydrogen. *Nat. Energy* **2019**, *4*, 216−222.

(3) Staffell, I.; Scamman, D.; Abad, V.; Balcombe, P.; Dodds, P. E.; Ekins, P.; Shah, N.; Ward, K. R. The Role of Hydrogen and Fuel Cells in the Global Energy System. *Energy Environ. Sci.* **2019**, *12*, 463−491.

(4) Carmo, M.; Fritz, D. L.; Mergel, J.; Stolten, D. A Comprehensive Review on PEM Water Electrolysis. *Int. J. Hydrogen Energy* **2013**, *38*, 4901−4934.

(5) Reier, T.; Nong, H. N.; Teschner, D.; Schlögl, R.; Strasser, P. Electrocatalytic Oxygen Evolution Reaction in Acidic Environments - Reaction Mechanisms and Catalysts. *Adv. Energy Mater.* **2017**, *7*, 1601275.

(6) Schalenbach, M.; Tjarks, G.; Carmo, M.; Lueke, W.; Mueller, M.; Stolten, D. Acidic or Alkaline? Towards a New Perspective on the Efficiency of Water Electrolysis. *J. Electrochem. Soc.* **2016**, *163* (11), F3197−F3208.

(7) Scholz, J.; Risch, M.; Wartner, G.; Luderer, C.; Roddatis, V.; Jooss, C. Tailoring the Oxygen Evolution Activity and Stability Using Defect Chemistry. *Catalysts* **2017**, *7* (5), 139.

(8) González-Huerta, R. G.; Ramos-Sánchez, G.; Balbuena, P. B. Oxygen Evolution in Co-Doped RuO_2 and IrO_2: Experimental and Theoretical Insights to Diminish Electrolysis Overpotential. *J. Power Sources* **2014**, *268*, 69−76.

(9) Gong, M.; Dai, H. A Mini Review of NiFe-Based Materials as Highly Active Oxygen Evolution Reaction Electrocatalysts. *Nano Res.* **2015**, *8* (1), 23−39.

(10) Fominykh, K.; Chernev, P.; Zaharieva, I.; Sicklinger, J.; Stefanic, G.; Döblinger, M.; Müller, A.; Pokharel, A.; Böcklein, S.; Scheu, C.; Bein, T.; Fattakhova Rohlfing, D. Iron-Doped Nickel Oxide Nanocrystals as Highly Efficient Electrocatalysts for Alkaline Water Splitting. *ACS Nano* **2015**, *9* (5), 5180−5188.

(11) Jamesh, M.; Sun, X. Recent Progress on Earth Abundant Electrocatalysts for Oxygen Evolution Reaction (OER) in Alkaline Medium to Achieve Efficient Water Splitting - A Review. *J. Power Sources* **2018**, *400*, 31−68.

(12) Trotochaud, L.; Ranney, J. K.; Williams, K. N.; Boettcher, S. W. Solution-Cast Metal Oxide Thin Film Electrocatalysts for Oxygen Evolution. *J. Am. Chem. Soc.* **2012**, *134*, 17253−17261.

(13) Wang, H.; Hsu, Y.; Chen, R.; Chan, T.; Chen, H. M.; Liu, B. Ni^{3+}-Induced Formation of Active NiOOH on the Spinel Ni - Co Oxide Surface for Efficient Oxygen Evolution Reaction. *Adv. Energy Mater.* **2015**, *5*, 1500091.

(14) Wygant, B. R.; Kawashima, K.; Mullins, B. Catalyst or Precatalyst? The Effect of Oxidation on Transition Metal Carbide, Pnictide, and Chalcogenide Oxygen Evolution Catalysts. *ACS Energy Lett.* **2018**, *3* (3), 2956−2966.

(15) Kuai, C.; Zhang, Y.; Han, L.; Xin, H. L.; Sun, C.; Nordlund, D.; Qiao, S.; Du, X.; Lin, F. Creating Compressive Stress at the NiOOH/NiO Interface for Water Oxidation †. *J. Mater. Chem. A* **2020**, *8* (8), 10747.

(16) Hwang, J.; Rao, R. R.; Giordano, L.; Katayama, Y.; Yu, Y.; Shao-Horn, Y. Perovskites in Catalysis and Electrocatalysis. *Science* **2017**, *358*, 751−756.

(17) Bockris, J. O. M.; Otagawa, T. The Electrocatalysis of Oxygen Evolution on Perovskites. *J. Electrochem. Soc.* **1984**, *131* (2), 290−302.

(18) Rincón, R. A.; Ventosa, E.; Tietz, F.; Masa, J.; Seisel, S.; Kuznetsov, V.; Schuhmann, W. Evaluation of Perovskites as Electrocatalysts for the Oxygen Evolution Reaction. *ChemPhysChem* **2014**, *15*, 2810−2816.

(19) Bockris, J. O. M.; Otagawa, T. Mechanism of Oxygen Evolution on Perovskites. *J. Phys. Chem.* **1983**, *87* (15), 2960−2971.

(20) Man, I. C.; Su, H.-Y. Y.; Calle-Vallejo, F.; Hansen, H. A.; Martínez, J. I.; Inoglu, N. G.; Kitchin, J.; Jaramillo, T. F.; Nørskov, J. K.; Rossmeisl, J. Universality in Oxygen Evolution Electrocatalysis on Oxide Surfaces. *ChemCatChem* **2011**, *3*, 1159−1165.

(21) Suntivich, J.; May, K. J.; Gasteiger, H. A.; Goodenough, J. B.; Shao-Horn, Y. A Perovskite Oxide Optimized for Oxygen Evolution Catalysis from Molecular Orbital Principles. *Science* **2011**, *334*, 1383−1385.

(22) Pittkowski, R.; Krtil, P.; Rossmeisl, J. Rationality in the New Oxygen Evolution Catalyst Development. *Curr. Opin. Electrochem.* **2018**, *12*, 218.

(23) Tiwari, S. K.; Koenig, J. F.; Poillerat, G.; Chartier, P.; Singh, R. N. Electrocatalysis of Oxygen Evolution/reduction on $LaNiO_3$ Prepared by a Novel Malic Acid-Aided Method. *J. Appl. Electrochem.* **1997**, *28*, 114−119.

(24) Singh, R. N.; Tiwari, S. K.; Singh, S. P.; Jain, A. N.; Singh, N. K. Electrocatalytic Activity of High Specific Surface Area Perovskite-Type $LaNiO_3$ via Sol-Gel Route for Electrolytic Oxygen Evolution in Alkaline Solution. *Int. J. Hydrogen Energy* **1997**, *22* (6), 557−562.

(25) El Baydi, M.; Tiwari, S. K.; Singh, R. N.; Rehspringer, J.-L.; Chartier, P.; Koenig, J. F.; Poillerat, G. High Specific Surface Area Nickel Mixed Oxide Powders $LaNiO_3$ (Perovskite) and $NiCo_2O_4$ (Spinel) via Sol-Gel Type Routes for Oxygen Electrocatalysis in Alkaline Media. *J. Solid State Chem.* **1995**, *116*, 157−169.

(26) Singh, R. N.; Jain, A. N.; Tiwari, S. K.; Poillerat, G.; Chartier, P. Physicochemical and Electrocatalytic Properties of $LaNiO_3$ Prepared

by a Low-Temperature Route for Anode Application in Alkaline Water Electrolysis. *J. Appl. Electrochem.* **1995**, *25*, 1133−1138.

(27) Soares, C. O.; Carvalho, M. D.; Melo Jorge, M. E.; Gomes, A.; Silva, R. A.; Rangel, C. M.; da Silva Pereira, M. I. High Surface Area $LaNiO_3$ Electrodes for Oxygen Electrocatalysis in Alkaline Media. *J. Appl. Electrochem.* **2012**, *42*, 325−332.

(28) Hardin, W. G.; Slanac, D. A.; Wang, X.; Dai, S.; Johnston, K. P.; Stevenson, K. J. Highly Active, Nonprecious Metal Perovskite Electrocatalysts for Bifunctional Metal - Air Battery Electrodes. *J. Phys. Chem. Lett.* **2013**, *4*, 1254−1259.

(29) Zhou, W.; Sunarso, J. Enhancing Bi-Functional Electrocatalytic Activity of Perovskite by Temperature Shock: A Case Study of $LaNiO_{3-\Delta}$. *J. Phys. Chem. Lett.* **2013**, *4*, 2982−2988.

(30) Petrie, J. R.; Cooper, V. R.; Freeland, J. W.; Meyer, T. L.; Zhang, Z.; Lutterman, D. A.; Lee, H. N. Enhanced Bifunctional Oxygen Catalysis in Strained $LaNiO_3$ Perovskites. *J. Am. Chem. Soc.* **2016**, *138*, 2488−2491.

(31) Qiu, Y.; Gao, R.; Yang, W.; Huang, L.; Mao, Q.; Yang, J.; Sun, L.; Hu, Z.; Liu, X. Understanding the Enhancement Mechanism of A-Site-Deficient La_xNiO_3 as an Oxygen Redox Catalyst. *Chem. Mater.* **2020**, *32*, 1864−1875.

(32) Wang, L.; Stoerzinger, K. A.; Chang, L.; Zhao, J.; Li, Y.; Tang, C. S.; Yin, X.; Bowden, M. E.; Yang, Z.; Guo, H.; You, L.; Guo, R.; Wang, J.; Ibrahim, K.; Chen, J.; Rusydi, A.; Wang, J.; Chambers, S. A.; Du, Y. Tuning Bifunctional Oxygen Electrocatalysts by Changing the A-Site Rare-Earth Element in Perovskite Nickelates. *Adv. Funct. Mater.* **2018**, *28*, 1803712.

(33) Liu, J.; Jia, E.; Wang, L.; Stoerzinger, K. A.; Zhou, H.; Tang, C. S.; Yin, X.; He, X.; Bousquet, E.; Bowden, M. E.; Wee, A. T. S.; Chambers, S. A.; Du, Y. Tuning the Electronic Structure of $LaNiO_3$ through Alloying with Strontium to Enhance Oxygen Evolution Activity. *Adv. Sci.* **2019**, *6*, 1901073.

(34) Zhang, D.; Song, Y.; Du, Z.; Wang, L.; Li, Y.; Goodenough, J. B. Active $LaNi_{1-x}Fe_xO_3$ Bifunctional Catalysts for Air Cathodes in Alkaline Media. *J. Mater. Chem. A* **2015**, *3*, 9421−9426.

(35) Costa, A.; Melo Jorge, M. E.; Carvalho, M. D.; Gomes, A.; da Silva Pereira, M. I. $LaNi_{1-x}Cu_xO_3$ (x = 0.05, 0.10, 0.30) Coated Electrodes for Oxygen Evolution in Alkaline Medium. *J. Solid State Electrochem.* **2013**, *17*, 2311−2318.

(36) Du, Z.; Yang, P.; Wang, L.; Lu, Y.; Goodenough, J. B.; Zhang, J.; Zhang, D. Electrocatalytic Performances of $LaNi_{1-x}Mg_xO_3$ Perovskite Oxides as Bi-Functional Catalysts for Lithium Air Batteries. *J. Power Sources* **2014**, *265*, 91−96.

(37) Nguyen, T. D.; Scherer, G. G.; Xu, Z. J. A Facile Synthesis of Size-Controllable IrO_2 and RuO_2 Nanoparticles for the Oxygen Evolution Reaction. *Electrocatalysis* **2016**, *7*, 420−427.

(38) Liu, J.; Römer, I.; Tang, S. V. Y.; Valsami-Jones, E.; Palmer, R. E. Crystallinity Depends on Choice of Iron Salt Precursor in the Continuous Hydrothermal Synthesis of Fe-Co Oxide Nanoparticles. *RSC Adv.* **2017**, *7*, 37436−37440.

(39) Fominykh, K.; Feckl, J. M.; Sicklinger, J.; Döblinger, M.; Böcklein, S.; Ziegler, J.; Peter, L.; Rathousky, J.; Scheidt, E. W.; Bein, T.; Fattakhova Rohlfing, D. Ultrasmall Dispersible Crystalline Nickel Oxide Nanoparticles as High-Performance Catalysts for Electrochemical Water Splitting. *Adv. Funct. Mater.* **2014**, *24*, 3123−3129.

(40) McBean, C. L.; Liu, H.; Scofield, M. E.; Li, L.; Wang, L.; Bernstein, A.; Wong, S. S. Generalizable, Electroless, Template-Assisted Synthesis and Electrocatalytic Mechanistic Understanding of Perovskite $LaNiO_3$ Nanorods as Viable, Supportless Oxygen Evolution Reaction Catalysts in Alkaline Media. *ACS Appl. Mater. Interfaces* **2017**, *9*, 24634−24648.

(41) Chen, Z.; Kronawitter, C. X.; Koel, B. E. Facet-Dependent Activity and Stability of Co_3O_4 Nanocrystals towards the Oxygen Evolution Reaction. *Phys. Chem. Chem. Phys.* **2015**, *17*, 29387−29393.

(42) Stoerzinger, K. A.; Diaz-Morales, O.; Kolb, M.; Rao, R. R.; Frydendal, R.; Qiao, L.; Wang, X. R.; Halck, N. B.; Rossmeisl, J.; Hansen, H. A.; Vegge, T.; Stephens, I. E. L.; Koper, M. T. M.; Shao Horn, Y. Orientation-Dependent Oxygen Evolution on RuO_2 without Lattice Exchange. *ACS Energy Lett.* **2017**, *2*, 876−881.

(43) Kakizaki, H.; Ooka, H.; Hayashi, T.; Yamaguchi, A.; Bonnet-Mercier, N.; Hashimoto, K.; Nakamura, R. Evidence That Crystal Facet Orientation Dictates Oxygen Evolution Intermediates on Rutile Manganese Oxide. *Adv. Funct. Mater.* **2018**, *28*, 1706319.

(44) Wu, J.; Liu, M.; Chatterjee, K.; Hackenberg, K. P.; Shen, J.; Zou, X.; Yan, Y.; Gu, J.; Yang, Y.; Lou, J.; Ajayan, P. M. Exfoliated 2D Transition Metal Disulfides for Enhanced Electrocatalysis of Oxygen Evolution Reaction in Acidic Medium. *Adv. Mater. Interfaces* **2016**, *3*, 1500669.

(45) Yu, X.; Mitoudi-Vagourdi, E.; Johnsson, M. The Aurivillius Compound $CoBi_2O_2F_4$ - an Efficient Catalyst for Electrolytic Water Oxidation after Liquid Exfoliation. *ChemCatChem* **2019**, *11*, 6105–6110.

(46) Song, F.; Hu, X. Exfoliation of Layered Double Hydroxides for Enhanced Oxygen Evolution Catalysis. *Nat. Commun.* **2014**, *5*, 4477.

(47) McAteer, D.; Godwin, I. J.; Ling, Z.; Harvey, A.; He, L.; Boland, C. S.; Vega-Mayoral, V.; Szydłowska, B.; Rovetta, A. A.; Backes, C.; Boland, J. B.; Chen, X.; Lyons, M. E. G.; Coleman, J. E. Liquid Exfoliated $Co(OH)_2$ Nanosheets as Low-Cost, Yet High-Performance, Catalysts for the Oxygen Evolution Reaction. *Adv. Energy Mater.* **2018**, *8*, 1702965.

(48) Tretyakov, Y. D.; Shlyakhtin, O. A. Recent Progress in Cryochemical Synthesis of Oxide Materials. *J. Mater. Chem.* **1999**, *9*, 19–24.

(49) Petrykin, V.; Macounova, K.; Shlyakhtin, O. A.; Krtil, P. Tailoring the Selectivity for Electrocatalytic Oxygen Evolution on Ruthenium Oxides by Zinc Substitution. *Angew. Chem., Int. Ed.* **2010**, *49*, 4813–4815.

(50) Nørskov, J. K.; Rossmeisl, J.; Logadottir, A.; Lindqvist, L.; Kitchin, J. R.; Bligaard, T.; Jónsson, H. Origin of the Overpotential for Oxygen Reduction at a Fuel-Cell Cathode. *J. Phys. Chem. B* **2004**, *108* (46), 17886–17892.

(51) Rossmeisl, J.; Qu, Z. W.; Zhu, H.; Kroes, G. J.; Nørskov, J. K. Electrolysis of Water on Oxide Surfaces. *J. Electroanal. Chem.* **2007**, *607*, 83–89.

(52) Klusackova, M.; Nebel, R.; Macounova, K. M.; Klementova, M.; Krtil, P. Size Control of the Photo-Electrochemical Water Splitting Activity of $SrTiO_3$ Nano-Cubes. *Electrochim. Acta* **2019**, *297*, 215–222.

(53) Macounová, K. M.; Nebel, R.; Klusáčková, M.; Klementová, M.; Krtil, P. Selectivity Control of the Photo-Catalytic Water Oxidation on $SrTiO_3$ Nanocubes via Surface Dimensionality. *ACS Appl. Mater. Interfaces* **2019**, *11* (18), 16506–16516.

(54) Zhu, Y.; Tahini, H. A.; Hu, Z.; Chen, Z.-G.; Zhou, W.; Komarek, A. C.; Lin, Q.; Lin, H.-J.; Chen, C.-T.; Zhong, Y.; Fernande-Diaz, M. T.; Smith, S. C.; Wang, H.; Liu, M.; Shao, Z. Boosting Oxygen Evolution Reaction by Creating Both Metal Ion and Lattice-Oxygen Active Sites in a Complex Oxide. *Adv. Mater.* **2020**, *32*, 1905025.

(55) Singh, S.; Prestat, E.; Huang, L.; Rondinelli, J. M.; Haigh, S. J.; Rosen, B. A. Role of 2D and 3D Defects on the Reduction of $LaNiO_3$ Nanoparticles for Catalysis. *Sci. Rep.* **2017**, *7*, 10080.

(56) Singh, S.; Zubenko, D.; Rosen, B. A. Influence of $LaNiO_3$ Shape on Its Solid-Phase Crystallization into Coke-Free Reforming Catalysts. *ACS Catal.* **2016**, *6*, 4199–4205.

(57) Woolley, R. J.; Illy, B. N.; Ryan, P.; Skinner, S. J. In Situ Determination of the Nickel Oxidation State in $La_2NiO_{(4+\delta)}$ and $La_4Ni_3O_{(10-\delta)}$ Using X-Ray Absorption near-Edge Structure. *J. Mater. Chem.* **2011**, *21*, 18592–18596.

(58) Anspoks, A.; Kuzmin, A.; Kalinko, A.; Timoshenko, J. Probing NiO Nanocrystals by EXAFS Spectroscopy. *Solid State Commun.* **2010**, *150*, 2270–2274.

(59) Gonzalez-Flores, D.; Klingan, K.; Chernev, P.; Loos, S.; Mohammadi, M. R.; Pasquini, C.; Kubella, P.; Zaharieva, I.; Smith, R. D. L.; Dau, H. Nickel-Iron Catalysts for Electrochemical Water Oxidation - Redox Synergism Investigated by in Situ X-Ray Spectroscopy with Millisecond Time Resolution. *Sustain. Energy Fuels* **2018**, *2*, 1986–1994.

(60) Mansour, A. N.; Melendres, C. A. XAFS Investigation of the Structure and Valency of Nickel in Some Oxycompounds. *Phys. B* **1995**, *208–209*, 583–584.

(61) Zhang, R.; Pearce, P. E.; Pimenta, V.; Cabana, J.; Li, H.; Dalla Corte, D. A.; Abakumov, A. M.; Rousse, G.; Giaume, D.; Deschamps, M.; Grimaud, A. First Example of Protonation of Ruddlesden-Popper Sr_2IrO_4: A Route to Enhanced Water Oxidation Catalysts. *Chem. Mater.* **2020**, *32* (8), 3499–3509.

(62) Chai, B.; Yoo, H.; Pollack, G. H. Effect of Radiant Energy on Near-Surface Water. *J. Phys. Chem. B* **2009**, *113* (42), 13953–13958.

(63) Oh, N. K.; Lee, H. J.; Choi, K.; Seo, J.; Kim, U.; Lee, J.; Choi, Y.; Jung, S.; Lee, J. H.; Shin, H. S.; Park, H. Nafion-Mediated Liquid-Phase Exfoliation of Transition Metal Dichalcogenides and Direct Application in Hydrogen Evolution Reaction. *Chem. Mater.* **2018**, *30* (14), 4658–4666.

(64) Mortensen, J. J.; Hansen, L. B.; Jacobsen, K. W. Real-Space Grid Implementation of the Projector Augmented Wave Method. *Phys. Rev. B: Condens. Matter Mater. Phys.* **2005**, *71* (3), 35109.

(65) Enkovaara, J.; Rostgaard, C.; Mortensen, J. J.; Chen, J.; Dułak, M.; Ferrighi, L.; Gavnholt, J.; Glinsvad, C.; Haikola, V.; Hansen, H. A.; Kristoffersen, H. H.; Kuisma, M.; Larsen, A. H.; Lehtovaara, L.; Ljungberg, M.; Lopez-Acevedo, O.; Moses, P. G.; Ojanen, J.; Olsen, T.; Petzold, V.; Romero, N. A.; Stausholm-Møller, J.; Strange, M.; Tritsaris, G. A.; Vanin, M.; Walter, M.; Hammer, B.; Häkkinen, H.; Madsen, G. K. H.; Nieminen, R. M.; Nørskov, J. K.; Puska, M.; Rantala, T. T.; Schiøtz, J.; Thygesen, K. S.; Jacobsen, K. W. Electronic Structure Calculations with {GPAW}: A Real-Space Implementation of the Projector Augmented-Wave Method. *J. Phys.: Condens. Matter* **2010**, *22* (25), 253202.

(66) Hjorth Larsen, A.; Jørgen Mortensen, J.; Blomqvist, J.; Castelli, I. E.; Christensen, R.; Dułak, M.; Friis, J.; Groves, M. N.; Hammer, B.; Hargus, C.; Hermes, E. D.; Jennings, P. C.; Jensen, P. B.; Kermode, J.; Kitchin, J. R.; Kolsbjerg, E. L.; Kubal, J.; Kaasbjerg, K.; Lysgaard, S.; Maronsson, J. B.; Maxson, T.; Olsen, T.; Pastewka, L.; Peterson, A.; Rostgaard, C.; Schiøtz, J.; Schütt, O.; Strange, M.; Thygesen, K. S.; Vegge, T.; Vilhelmsen, L.; Walter, M.; Zeng, Z.; Jacobsen, K. W. The Atomic Simulation Environment—a Python Library for Working with Atoms. *J. Phys.: Condens. Matter* **2017**, *29* (27), 273002.

(67) Perdew, J. P.; Burke, K.; Ernzerhof, M. Generalized Gradient Approximation Made Simple. *Phys. Rev. Lett.* **1996**, *77* (18), 3865–3868.

(68) Wellendorff, J.; Lundgaard, K. T.; Møgelhøj, A.; Petzold, V.; Landis, D. D.; Nørskov, J. K.; Bligaard, T.; Jacobsen, K. W. Density Functionals for Surface Science: Exchange-Correlation Model Development with Bayesian Error Estimation. *Phys. Rev. B: Condens. Matter Mater. Phys.* **2012**, *85* (23), 235149.

(69) Abbott, D. F.; Pittkowski, R. K.; Macounová, K.; Nebel, R.; Marelli, E.; Fabbri, E.; Castelli, I. E.; Krtil, P.; Schmidt, T. J. Design and Synthesis of Ir/Ru Pyrochlore Catalysts for the Oxygen Evolution Reaction Based on Their Bulk Thermodynamic Properties. *ACS Appl. Mater. Interfaces* **2019**, *11* (41), 37748–37760.

(70) Doebelin, N.; Kleeberg, R. Profex: A Graphical User Interface for the Rietveld Refinement Program BGMN. *J. Appl. Crystallogr.* **2015**, *48* (5), 1573–1580.

(71) Hÿtch, M. J.; Snoeck, E.; Kilaas, R. Quantitative measurement of displacement and strain fields from HREM micrographs. *Ultramicroscopy* **1998**, *74*, 131–146.

(72) Klinger, M. More features, more tools, more CrysTBox. *J. Appl. Crystallogr.* **2017**, *50*, 1226–1234.

(73) Newville, M. IFEFFIT: Interactive XAFS Analysis and FEFF Fitting. *J. Synchrotron Radiat.* **2001**, *8*, 322–324.

(74) Ravel, B.; Newville, M. ATHENA, ARTEMIS, HEPHAESTUS: Data Analysis for X-Ray Absorption Spectroscopy Using IFEFFIT. *J. Synchrotron Radiat.* **2005**, *12*, 537–541.

(75) It should be noted that the term pair in the text addresses essentially the distance at which specific atoms appear in the structure and its use does not suggest a direct bond formation between these atoms.